Design of water gas shift catalysts for hydrogen production in fuel processors



2008 J. Phys.: Condens. Matter 20 064237

(http://iopscience.iop.org/0953-8984/20/6/064237)

J. Phys.: Condens. Matter **20** (2008) 064237 (12pp) doi:10.1088/0953-8984/20/6/064237

# Design of water gas shift catalysts for hydrogen production in fuel processors

**S M Opalka, T H Vanderspurt, R Radhakrishnan, Y She and R R Williган**

United Technologies Research Center, East Hartford, CT 06108, USA

E-mail: opalkasm@utrc.utc.com

Received 2 September 2007
Published 24 January 2008
Online at stacks.iop.org/JPhysCM/20/064237

**Abstract**

Low sulfur hydrocarbon fuels can be converted to fuel cell grade $H_2$ using a compact fuel processor architecture. The necessary high volumetric activity water gas shift (WGS) Pt on ceria–zirconia catalysts reacts CO-rich reformate with steam to yield $H_2$ and $CO_2$. Such highly selective, non-pyrophoric noble metal/$Ce_{[1-(x+y)]}Zr_xDp_yO_2$ catalysts were developed through coordinated atomic modeling, syntheses, structural characterization, kinetic performance tests, and micro-kinetic analyses. Density functional simulations made with the VASP code suggested that the undoped catalyst WGS activity would be limited by the strong binding of CO intermediates, blocking the reoxidation of the reduced oxide by water. These predictions were confirmed by *in situ* cylindrical internal reflection–Fourier transform infrared spectroscopy and by micro-kinetic analyses of the micro-reactor results. Atomic simulations were used to evaluate the impact transition metal dopants had on the surface chemistry of cubic ceria–zirconia. VASP predicted that acidic transition metal dopants such as Nb, Mo, Ta, and W would increase the oxide surface affinity for water and thus increase the turnover rate of the catalyst. The efficacy of Mo-doped ceria–zirconia compositions was confirmed at lower temperatures in replicated catalyst synthesis-reactor studies.

## 1. Introduction

Polymer electrolyte membrane fuel cell power systems require compact multistage fuel processing systems for the conversion of fossil or bio-derived hydrocarbon liquid feedstock to very high purity hydrogen fuel. In these systems, catalytic steam reforming, autothermal reforming, or catalytic partial oxidation is used to convert the raw hydrocarbon mixture to $H_2$ and CO-rich reformate. In the next stage(s), the reformate and injected steam undergo the water gas shift (WGS) reaction, $H_2O + CO \leftrightarrow H_2 + CO_2$. The WGS reaction is exothermic and equilibrium-limited at the high temperatures necessary for high catalytic activity. In compact fuel cell power plant fuel processors the first WGS stage has an exit temperature of ~400 °C and reduces the CO concentration to >2%. This is followed by a heat exchanger to drop to the second WGS stage inlet temperature of ~100 °C or more. The second WGS stage, often physically larger than the first WGS stage, reduces the CO concentration to levels that can be tolerated by the downstream preferential oxidation unit(s), typically <0.6%. Employing a WGS catalyst that maintains high volumetric activity at lower temperatures cannot only reduce overall reactor size but can even eliminate one of the two preferential oxidation stages. For some WGS catalysts, like the older Cu–$ZnO_2$ type, the WGS rate is proportional to the CO partial pressure to the first order. This means that reducing the CO concentration from 1% to 0.5% requires twice as much catalyst as reducing it from 2% to 1%, thus leading to large second stage WGS reactors. The objective of our work was to identify cost effective catalysts that were tolerant to O exposure, had robust, high volumetric activities at lower temperatures, and whose rate was independent of the CO concentration (zero order) between ~2 and 0.25%.

Noble metal supported ceria-based catalysts are known for their tolerance to O exposure, that is they are not dangerously pyrophoric in the reduced form. Some noble metal ceria catalysts were reported to have attractive volumetric activity that was zero order in CO concentration [1]. Others believed that these materials lacked the robustness for practical fuel cell–fuel processor WGS applications. We undertook the challenge of developing a practical WGS system through a coordinated effort employing atomistic modeling,

 

the self-assembly of nanoscale complex oxides, materials characterization, kinetic performance tests, and micro-kinetic analyses. The result was a family of high Pt-alloy/ceria–zirconia WGS catalysts having high volumetric activity [2–7]. These catalysts contained ceria–zirconia nanocrystallites with diameters of less than 4 nm, that are aggregated to form ∼0.1 $\mu$m particles having pores in the range of 4 to about 9 nm, with larger pores up to hundreds of microns in diameter between the particles [2]. The resulting fractal pore structure provided for low internal mass transfer resistance and a large effective active surface area. The catalysts were reducible at low temperatures $<100\,^{\circ}$C. The catalysts contained Pt clusters that were too small to be detected by XRD or directly imaged by TEM, and which were measured to be ∼100% dispersed by CO chemisorption [2].

There are a number of proposed WGS mechanisms for these Pt–$CeO_2$ catalysts [1, 8–11]. The mechanism that is the most consistent with our experimental and kinetic testing results is called the bimolecular or the regenerative mechanism [1, 8]. Here, carbon monoxide reacts at the interface between the platinum and ceria, with surface species in equilibrium with the moist reactor atmosphere. Oxygen is abstracted from the adjacent ceria lattice to oxidize the CO to $CO_2$, locally reducing two $Ce^{4+}$ ions to the $Ce^{3+}$ state. The resulting reduced ceria lattice is then reoxidized through the dissociation of incoming $H_2O$. The O vacancy is then refilled, formally oxidizing two $Ce^{3+}$ to $Ce^{4+}$ and releasing molecular $H_2$ in the process. This mechanism requires both O and electronic conduction. In the ideal case, the adsorbates do not compete with each other for the same sites, so that zero order rate dependence for CO is predicted. However, our WGS kinetic models obtained for Pt/cubic $Ce_{(1-x)}Zr_xO_2$ showed that the bimolecular mechanism did not completely describe our catalyst behavior. Another associative mechanism has been proposed to only occur on oxide surface sites. Here, the adsorbed carbon monoxide and $H_2O$ combine to form a formate (HCOO) or related ligand complex [9], with first order rate dependencies for CO and $H_2O$. This complex can be displaced by incoming $H_2O$ and can decompose to form $CO_2$ and $H_2$. Alternatively, it can partially decompose to form carbonate ($CO_3^{2-}$) or carboxylate (COOH) reaction products. Formate or carbonate species can block active surface sites for the reoxidation of the reduced oxide.

At the outset, we observed evidence to support the simultaneous occurrence of both the associative and bimolecular mechanisms on our Pt/ceria-based catalysts. Under low temperature and high $H_2O$ concentration WGS reactor conditions, our preliminary CO conversion rates were best described by kinetics that approached zero order dependence for CO and first order dependence for $H_2O$, typical of the regenerative mechanism. At the same time, we observed CO-based intermediates dominated $Ce_{(1-x)}Zr_xO_2$ surfaces under low temperature WGS reaction conditions by cylindrical internal reflectance–Fourier transform infrared spectroscopy (CIR–FTIR) [7]. With these combined observations, we hypothesized that the associative complexation of reduced oxide surface blocked the regenerative reoxidation from $H_2O$ dissociation, and thus limited the turnover of catalytic sites to less than optimum performance. We used the materials discovery paradigm of integrating VASP density functional simulations with advanced inorganic syntheses, characterizations, kinetic performance tests, and micro-kinetic reaction analyses, to provide insight into experimental findings and to guide the optimization of catalytic activity. This approach was used to successfully reformulate the ceria–zirconia oxide supports by doping with certain transition metal (TM) ions to favor the adsorption of water on the oxide surface and to shift the reoxidation equilibrium to enhance the regenerative mechanism.

## 2. Methodology

Ceria and mixed Ce/Zr oxide bulk and surface slabs, adsorbate molecules, and combined slab-adsorbate ionic and electronic structures were simulated on a plane-wave, periodic basis with the density functional theory (DFT) Vienna *Ab Initio* Simulation Package (VASP) code [12–14]. High precision ground state minimizations were made using projector augmented wave potentials (PAW) [15] with the generalized gradient approximation exchange–correlation functional of Perdew and Wang 91 [16]. The ionic minimizations were made with the conjugate gradient method, achieving electronic convergence in each ionic iteration with the residual minimization method–direct inversion in iterative subspace (RMM-DIIS) method and real wavefunction projections. All atoms in this study were represented with regular PAW potentials (including Ce, O, H, C, Mo, W), with the exception that hard potentials were selected for (element (designation)): Zr (Zr_sv), Nb (Nb_pv), and Ta (Ta_pv). Although all calculations were made with paired electron spins for computational efficiency, spot-checks were made with spin-polarized calculations to ensure the reliability of using non-spin polarization to describe surface reaction behavior. All calculations were made with energy converged parameters, including the plane-wave cutoff of 400 eV, 0.5 $Å^{-1}$ $k$-point meshes, and Fermi smearing with an energy broadening of 0.2 eV, and a final energy extrapolation to zero smearing. The relaxation criterion for atomic force convergence was 0.05 eV $Å^{-1}$.

By deploying PAW potentials in our calculations, we were able to simulate cubic ($Fm\bar{3}m$) $CeO_2$ lattice properties in excellent agreement with reported experimental values. By selecting the 12 electron $\{5s^2 5p^6\ 5d^1\ 4f^1\ 6s^2\}$ Ce PAW GGA potential with 4f electronic states incorporated into the valence band, we predicted the cubic lattice parameter within 0.1% [17], the lattice energy within 2% [18], and the bulk modulus within 14% [19] of the nominal $CeO_2$ experimental values. As is commonly reported for other systems, the use of linear density approximation (LDA) for exchange–correlation improved our predicted bulk modulus to within 0.5% of the experimental value. Our overall high level of agreement with experimental values exceeded that reported for other simulation methodologies [20–23]. This demonstrated reliability served to bolster our confidence in implementing modeling alongside catalysis experimentation. The results also supported using the 4f orbital valence band model for

describing mixed ionic-covalent bonding in $CeO_2$, where Ce participates in both tetravalent ionic bonding interactions and localized O 2p and Ce 4f orbital covalent interactions, leading to fractional 4f orbital occupation [23, 24]. The impact of this model on the electronic state of $CeO_2$ is significant, where the Ce 4f electronic states actually straddle the band gap and are thus likely to provide highest occupied molecular orbitals (HOMO) and/or lowest unoccupied molecular orbitals (LUMO) for participation in chemical reactions.

Our main impetus for instituting atomic-scale DFT modeling in our catalysis research was that our experimental phenomena of interest were very close in length-scale to tractable-size models which could be effectively processed by the VASP code with our available computational facilities. We routinely synthesize fractal geometry, high surface area, nanoscale ceria–zirconia crystallites by precipitation from dilute solutions. Fluorite structures, such as $CeO_2$, commonly occur as crystallites that maximize the most stable {111} surface formation. During precipitation, the nanocrystallites cluster through interaction of the less stable, highly reactive faces, to form high surface area aggregates, leaving lower energy faces available to support WGS reactions. For this reason, we selected the (111) surface for the simulation of WGS reactions on our catalysts. The (111) slabs were constructed by first recasting the periodic net in the [111] direction of the ceria-based fluorite lattice and then defining a 36 atom: 12 cation and 24 O anion ($a\sqrt{2} \times a\sqrt{2} \times a\sqrt{3}$) repeating unit basis, where '$a$' equals the minimized fluorite cubic cell lattice parameter, 5.417 Å. Full cell minimizations, the relaxation of lattice parameters, angles, and atomic positions, were implemented to determine ground state bulk structures for undoped ceria and mixed ceria–zirconia compositions (given in atomic formula): $Ce_{0.83}Zr_{0.17}O_2$, $Ce_{0.67}Zr_{0.33}O_2$, $Ce_{0.58}Zr_{0.42}O_2$, and $Ce_{0.50}Zr_{0.50}O_2$. Each mixed ceria–zirconia composition was represented by a single ionic configuration formed by substituting Zr as randomly as possible for Ce, where the redefined $CeO_2$ ($a\sqrt{2} \times a\sqrt{2} \times a\sqrt{3}$) repeating unit basis enabled substitution stoichiometries to be formed that closely matched our experimental compositions. Further bulk minimizations were made after substituting one Nb, Ta, Mo or W atom for one Ce or Zr atom in the intermediate $Ce_{0.58}Zr_{0.42}O_2$ composition. Minimized bulk lattice periodic structures were then cleaved to form (111) surface slabs by adding 10 Å of vacuum space to the $c$ lattice parameter, while keeping atomic positions fixed. The (111) doped slabs were cleaved so that the dopant was positioned in the top slab layer. The ionic positions of all slab structures were minimized with the energy converged bulk parameters except for the change to a single $k$-point in the surface-normal direction, while fixing the coordinates of the bottom of the three O–Ce–O layers to approximate bulk $CeO_2$ behavior. These slab models had enough (111) surface area to investigate surface reactions with minimal interactions between periodic repeats, enough depth (∼10 Å) to closely approximate the radius of our nanocrystallites (typically 10–15 Å), and the minimum number of stoichiometric layers necessary both to represent the fluorite symmetry in the [111] direction and to avoid a non-zero dipole moment perpendicular to the surface [20].

All minimized slab models invoked hydrated layers as an integral part of investigating WGS surface reactions in high $H_2O$ reactor environments. A full $H_2O$ monolayer (1 ML $H_2O$), or 1 $H_2O$ for each of four slab surface cations, was loaded on the slab surfaces and the slabs were ionically minimized. The WGS reaction intermediate steps were then systematically evaluated. First, surface reduction behavior was probed by removing a single O atom from various positions in the surface and subsurface layers and minimizing the ionic positions. Second, the adsorption behavior of CO, $CO_2$, and various possible associative formate and carbonate complexes were minimized and profiled on the hydrated surfaces.

## 3. Results and discussion

Our goal was to gain atomic insight into WGS reaction mechanisms that occur on our catalyst oxide support surfaces to intuitively guide experimental catalyst reformulation for improved performance. This required an iterative experimental-modeling approach; where experimentation was used to define the conditions for investigation and modeling was used to aid in experimental interpretation. In this manner, we were able to progressively build an understanding of mixed oxide hydration, oxidation–reduction behavior, and the change in WGS reaction mechanisms with dopant substitution. Although the primary objective of this report is to present atomic modeling results, they will be highlighted with key catalyst experimental synthesis, characterization and performance test results that have already been reported in detail elsewhere [2–7].

### *3.1. Mixed ceria–zirconia oxides*

For more than two decades, significant research efforts have been focused on substituting Zr to improve the activity and thermal stability of three way conversion (TWC) $CeO_2$ catalysts for reducing the toxicity of internal combustion emissions. The incorporation of Zr has been shown to also play an important role in promoting WGS catalyst activity and stability [8]. It has been shown that the cubic $CeO_2$ phase becomes tetragonal when Zr doping levels are at or above 15 wt% [25]. Several different tetragonal phases of varying degrees of stability can be formed depending upon the Zr doping level, preparation technique, crystallite size, texture, and thermal history [26]. The metastable $t''$ phase is commonly formed when Zr doping ranges from 15 to 28 wt%, which has a tetragonal O anion sublattice and a cubic Ce/Zr sublattice. These phases are indexed as cubic phases by powder x-ray diffraction (PXRD), because of the insensitivity of PXRD to the O sublattice. Another metastable $t'$ phase that can form between 28 and 63 wt% Zr doping, is tetragonal ($P4_2/nmc$ space group) on both sublattices having a $c/a$ lattice parameter ratio greater than unity [26]. We conducted PXRD and Raman spectroscopy to determine the bulk structure of the 2–3 nm diameter crystallites synthesized in our laboratory, with $CeO_2$:$ZrO_2$ weight% compositions ranging from 100:0 to 58:42. The PXRD results showed that our nanocrystallite lattice parameters followed the general trend predicted by the

**Table 1.** Comparison of experimental and theoretical ceria–zirconia data.

| Composition | | $Fm\bar{3}m$ lattice parameter $a$ (Å) | | |
|---|---|---|---|---|
| Atomic formula | $CeO_2$:$ZrO_2$ (wt%) | X-ray measured | Kim's rule estimated[a] | VASP predicted[b] |
| $CeO_2$ | 100:0 | 5.4157 | 5.4130 | 5.4170 |
| $Ce_{0.83}Zr_{0.17}O_2$ | 87:13 | 5.3880 | 5.3646 | 5.3718 |
| $Ce_{0.67}Zr_{0.33}O_2$ | 74:26 | 5.3592 | 5.3184 | 5.3161 |
| $Ce_{0.58}Zr_{0.42}O_2$ | 66:34 | 5.3289 | 5.3030 | 5.2894 |
| $Ce_{0.50}Zr_{0.50}O_2$ | 58:42 | 5.3053 | 5.2832 | 5.3445 |

[a] Kim's rule from [27]: $a = 5.413 - (0.00220 \text{ mol\% } ZrO_2)$.
[b] Estimated from minimized ($a\sqrt{2} \times a\sqrt{2} \times a\sqrt{3}$) cell: $a = [\text{cell volume}/(2\sqrt{3})]^{0.33}$.

well-known Kim's rule [27], however, they were consistently larger by up 0.04 Å. Our Raman results showed that the $CeO_2$ structure has the $t''$ symmetry throughout this compositional range, and did not follow the trends reported in the literature. It was our working hypothesis that the metastable $t''$ phase was stabilized in the nanocrystallites. This symmetry was even observed to be stable after elevated temperature calcinations at 650 °C.

Recent analyses have attributed the improved reducibility and O mobility in Ce–Zr mixed oxides to unique local structural features resulting from the dispersion of interatomic distances and reduction in Zr–O coordination number induced by the substitution of Zr in the $CeO_2$ lattice [22, 28, 29]. Table 1 shows our experimentally and theoretically determined lattice parameters for a range of ceria–zirconia nanocrystallite compositions. The average VASP ground state minimized lattice parameters followed Kim's rule [27] at the intermediate binary compositions, and exhibited a marked positive deviation at the extreme $Ce_{0.50}Zr_{0.50}O_2$ composition, representative of a monoclinic-type lattice distortion [30]. These distortions were manifested as doublet peak splittings for $Ce_{0.83}Zr_{0.17}O_2$ and $Ce_{0.58}Zr_{0.42}O_2$, and triplet peak splittings for all other mixed ceria–zirconia compositions in predicted PXRD from the minimized bulk structures. The predicted lattice parameter changes were due to dispersion of cation-O interatomic distances from the Ce–O 2.3457 Å interatomic distance in cubic $CeO_2$. The Ce–O and Zr–O interatomic distances spanned equivalent ranges in the intermediate $Ce_{0.83}Zr_{0.17}O_2$ composition, reflecting uniform lattice distributions without local distortions. In higher Zr-containing oxides, the cation-O interatomic distances broadened even further and were dependent upon the Zr distribution surrounding a given O ion.

### *3.2. Surface hydration*

In the high $H_2O$ content WGS reactors, as well as many other catalytic applications, $H_2O$ adsorbates dramatically alter the nature and reactivity of the catalyst surfaces [31, 32]. We have observed condensed $H_2O$ and hydroxyls on our ceria-based catalyst surfaces with CIR–FTIR spectroscopy under the high $H_2O$, elevated temperature WGS reactor conditions. There is very little fundamental understanding around the roles that the Ce d and f orbitals play in the surface bonding interactions. For these reasons, we sought to study $H_2O$ adsorption behavior on ceria-based oxide slab surfaces to serve as a basis for incorporating hydrated surface layers into our models. Following ground state minimization of Hellmann–Feynman forces for $H_2O$ on $CeO_2$ (111), the optimum adsorption configuration had the $H_2O$ molecular plane parallel to the surface and the $H_2O$ O ion aligned directly on top of a seven-coordinated surface Ce ion. This conformation has been observed for $H_2O$ on other soft oxides [33]. The density of states (DOS) analyses showed that $H_2O$ was adsorbing as a Lewis base by electrostatically donating electrons in the highest occupied molecular orbital (HOMO) $1b_1$ and intermediate energy $3\sigma$ molecular orbitals to interact and hybridize with Ce 4f and 5d orbitals. Hydration of the (111) surface Ce ion reestablished a valence of eight. The $H_2O$ hydrogen ions H-bonded with under-coordinated surface bridging O, causing the $H_2O$ $1b_2$ molecular orbitals to shift to lower energies in the bottom of the valence band. The surface stabilization by $H_2O$ adsorption was manifested as increased valence band hybridization and broadening in the DOS. The average ground state average $H_2O$ adsorption enthalpy, in kJ $mol^{-1}$ units, was determined as:

**Table 2.** Average $H_2O$ adsorption enthalpy, $\Delta H_{\text{ads } H_2O}$, for one monolayer $H_2O$ on (111) slabs.

| Atomic formula | $\Delta H_{\text{ads } H_2O}$ (kJ $mol^{-1}$ per $H_2O$) |
|---|---|
| $CeO_2$ | −52.4 |
| $Ce_{0.83}Zr_{0.17}O_2$ | −57.3 |
| $Ce_{0.67}Zr_{0.33}O_2$ | −54.7 |
| $Ce_{0.58}Zr_{0.42}O_2$ | −57.7 |
| $Ce_{0.50}Zr_{0.50}O_2$ | −31.9 |

$$\Delta H_{\text{ads } H_2O} = \frac{\{H_{\text{hydrated slab}} - [H_{\text{bare slab}} + (H_{H_2O} * \text{No. } H_2O \text{ adsorbed})]\}}{\{\text{No. } H_2O \text{ adsorbed}\}} \quad (1)$$

where all models were minimized in the same size periodic cells with the same calculation parameters. A $H_2O$ adsorption enthalpy of less than 0 represented a favorable, exothermic reaction. The moderate adsorption enthalpy of −47.3 kJ $mol^{-1}$ per isolated $H_2O$ molecule did not change significantly upon the formation of a full $H_2O$ monolayer [34]. The adsorbed $H_2O$ formed a regular ice-like configuration in the 1 ML $H_2O$, tilting to enable every $H_2O$ molecule to moderately H-bond with one surface O and to participate in a weak H-bond with an adjacent $H_2O$ O ion. Table 2 shows that the $H_2O$ adsorption enthalpy in the 1 ML $H_2O$ was −52.4 kJ $mol^{-1}$ per $H_2O$ molecule. The weak dependence of the $H_2O$ adsorption energy with coverage on $CeO_2$(111) is in agreement with prior simulations [35]. This adsorption enthalpy was intermediate in magnitude between the unfavorable adsorption enthalpy for basic MgO and the very favorable hydration enthalpy for $TiO_2$ [36].

The substitution of $ZrO_2$ in the $CeO_2$(111) slab models not only impacted the bulk lattice structure, but also altered the conformation of $H_2O$ adsorbates in the fully hydrated ML. In the minimized mixed ceria–zirconia (111) 1 ML $H_2O$ slab models, the $H_2O$ molecules did not adsorb as Lewis bases directly on top of the single Zr ions exposed at the surface,

**Table 3.** Reduction enthalpies, $\Delta H_{\text{reduction}}$, per O abstracted from bare slabs and (111) slabs with one monolayer $H_2O$.

| Composition Atomic formula | Reduction[a] enthalpy (kJ mol$^{-1}$ per O atom) | | |
|---|---|---|---|
| | O removal dissociated $H_2O$ | O removal formed surface vacancy | O removal formed subsurface vacancy |
| Bare slabs | | | |
| $CeO_2$ | — | 302.0 | Not stable |
| $Ce_{0.67}Zr_{0.33}O_2$ | — | Not stable | 209.4 |
| $Ce_{0.58}Zr_{0.42}O_2$ | — | Not stable | 333.5 |
| 1 ML hydrated slabs | | | |
| $CeO_2$ | 140.9 | 215.2 | 270.2 |
| $Ce_{0.67}Zr_{0.33}O_2$ | 224.8 | Not stable | 192.0 |
| $Ce_{0.58}Zr_{0.42}O_2$ | 174.1 | Not stable | 134.0 |

[a] Reduction: $Ce_{(1-x-y)}TM_{(y)}Zr_{(x)}O_2 * 4H_2O \rightarrow Ce_{(1-x-y)}TM_{(y)}Zr_{(x)}O_{1.92} * 4H_2O + \frac{1}{2}O_2$.

but were rather adsorbed as Brønsted acids onto an adjacent O atom, electrostatically interacting to form a lower energy $1b_2$ split-off state below the valence band. The lattice O complexation with $H_2O$ was stabilized by H-bonding with an adjacent $H_2O$ molecule, which was slightly displaced from the soft adsorption conformation on top of an adjacent surface Ce. Complexation of the under-coordinated surface O enabled the Zr to assume a stable seven-coordinated configuration with the surrounding O ions, and was reminiscent of monoclinic Zr–O coordination. Hydration of these oxide slab compositions resulted in increased valence band hybridization with an improved overlap between the Ce 5d and Zr 4d orbitals, and a lowering in energy of the Ce 4f orbitals. In these minimized binary compositions, there was not a significant change in the adsorption enthalpy per $H_2O$ molecule compared to pure $CeO_2$. However, the impact of the Zr substituent-induced alteration of binding conformations and intermolecular interactions on catalytic surface reactivity remained to be of interest.

### *3.3. Ceria–zirconia oxidation–reduction behavior*

It is well established that under low temperature and pressure WGS reactor conditions, O ions can be abstracted from noble metal loaded ceria-based oxides by reducing gases, and that the resulting vacancies can be replenished by oxidizing gases. The capacity of an oxide to undergo reduction–oxidation reactions with surrounding gaseous species is termed 'oxygen storage capacity (OSC)' [31]. OSC has been shown to play a strong role in enabling WGS regenerative reactions on noble metal promoted ceria-based oxides, in controlling both CO oxidation and bulk lattice reoxidation [1, 11]. It has been clearly shown that Zr substitution can have a dramatic effect on decreasing reduction energy [28], increasing the OSC [31] and decreasing reduction temperature [30] of ceria-based oxides. Noble metal loading plays an important role in promoting oxidation–reduction behavior of ceria-based catalysts. A moderate surface area (64 m$^2$ g$^{-1}$) $Pt/Ce_{0.5}Zr_{0.5}O_2$ was shown by temperature programmed reduction (TPR) studies to exhibit two reduction peaks at 350 and 750 °C [37]. Our own high surface area (∼200 m$^2$ g$^{-1}$) and highly dispersed (90%) Pt-loaded ceria-based nanocrystallites have exhibited even lower temperature reducibility. We have commonly observed a significant low TPR peak centered at 115 °C for a wide range of ceria–zirconia compositions.

Water plays important roles in OSC and WGS reactions, both as a source of surface groups that mitigate the oxide reactivity and O migration, and as the source of O for lattice reoxidation. For this reason, we have probed reduction-reoxidation coupled with the acid–base reactions of the hydrated surface layer as a basis for establishing a comprehensive regenerative WGS mechanism. The $CeO_2(111)$ surface is the lowest energy, most compact and highest coordinated of possible surfaces that can be formed from the fluorite lattice, and therefore will be the most energy intensive to reduce. We 'reduced' $CeO_2(111)$ slab models by removing neutral O ions at selected locations and conducting VASP ionic minimizations. The ground state reduction enthalpy was determined in kJ mol$^{-1}$ units as

$$\Delta H_{\text{reduction}} = H_{\text{reduced slab}} + \tfrac{1}{2}H_{\text{molecular O}_2} - H_{\text{oxidized slab}} = -\Delta H_{\text{reoxidation}}. \quad (2)$$

Here, a more positive reduction enthalpy indicated a less favorable or more endothermic reaction. In our hydrated models, table 3 shows that it was more favorable to form a $CeO_2(111)$ surface vacancy requiring the input of 215.2 kJ mol$^{-1}$ than to form a subsurface vacancy with the input of 270.2 kJ mol$^{-1}$. The preference of O vacancies to form at $CeO_2(111)$ surfaces has been seen both experimentally [31] and in simulations [38]. These reduction energies are in close agreement with thermodynamic results [39] and fall within the range of reported results for nearly identical methodologies [40, 41]. The higher 302.0 kJ mol$^{-1}$ endothermic input for the corresponding surface reduction of a bare $CeO_2(111)$ slab, sheds light on the role of the hydrated layer in promoting WGS reduction reactions. The hydrated layer alteration following reduction serves as evidence of these interactions. The surface vacancy induced the dissociation of one $H_2O$ molecule, resulting in the hydroxylation of a neighboring surface Ce ion and the protonation of a nearest neighbor O ion. The DOS analyses confirmed that the excess electron charge from the lattice reduction was locally transferred through the hybridization of the Ce 5d orbital with the hydroxyl O $1\pi$ orbital. It was also predicted that it was more favorable

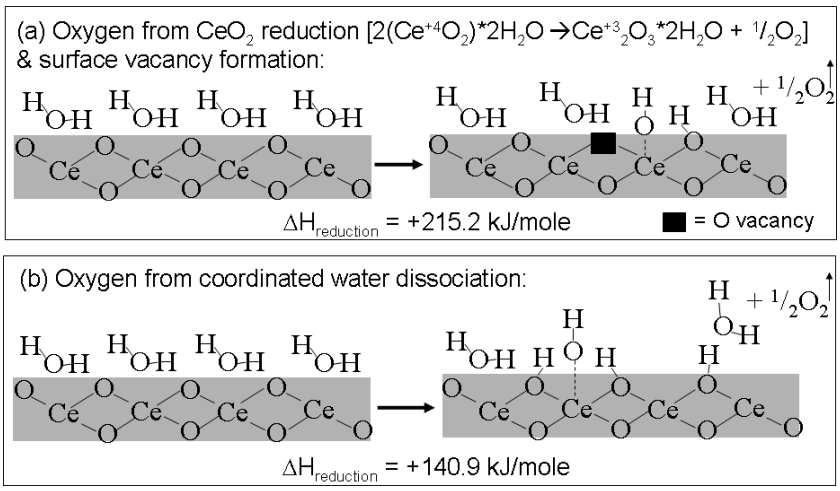


**Figure 1.** Reaction schematic for reduction of fully hydrated $CeO_2$ (111) surface with O abstraction (a) from surface vacancy formation and (b) from water dissociation.

to generate O from the dissociation of the overlying $H_2O$ adsorbates, than from the $CeO_2$ lattice itself. The favorable $H_2O$ decomposition intermediate revealed that O abstraction through the coordinated dissociation of two $H_2O$ molecules in the hydrated $CeO_2$ surface layer only required 140.9 kJ $mol^{-1}$ (refer to table 3), which was significantly less endothermic than the formation of the surface vacancy. Here, O removal prompted the protonation of three $CeO_2$ surface O and the formation of hydroxyl on top of a Ce atom. The protonated O's were stabilized by H-bonding interactions with the Ce hydroxyl and with remaining adjacent adsorbed $H_2O$ groups. The two $CeO_2$(111) reduction reactions are shown schematically for clarity in figure 1.

Our predictions revealed that the substitution of Zr for Ce altered the balance between lattice reduction and $H_2O$ reactions on the hydrated ceria-based (111) slabs. In our simulations of hydrated mixed ceria–zirconia (111) slabs, O abstraction from $H_2O$ dissociation was not as favorable as the formation of vacancies in the lattice. Oxygen abstraction from $H_2O$ decomposition required up to 224.8 kJ $mol^{-1}$, and caused the subsurface O between the resulting two protonated surface O's to migrate part-way towards the surface. The simulation results in table 3 predict that the substitution of Zr increased the favorability of lattice reduction. In contrast to the hydrated $CeO_2$(111) surface, surface vacancies did not correspond to a local potential energy minimum in the hydrated ceria–zirconia (111) surfaces. During minimization, the surface vacancies migrated to subsurface sites. Although ionic movements during minimization do not follow reaction pathways but rather follow a trajectory to lower model energies and forces, there are limited possible pathways for movement of O between cations [28]. For this reason, we speculate that the submergence of surface vacancies may actually be a manifestation of a spontaneous, non-activated diffusion process. Subsurface vacancy sites with less than two Zr neighbors were not stable and were reestablished at sites with two or more Zr neighbors. The distances between neighboring cations (especially the Ce–Zr and Zr–Zr distances) surrounding these vacancy sites were significantly enlarged, by up to 0.3 Å, following reduction. These vacancies all required up to ∼200 kJ $mol^{-1}$ input and did not appreciably alter the $H_2O$ conformations in the hydrated layer. However, formation of the most favorable vacancy in bare ceria–zirconia (111) slabs required higher energy inputs, reaffirming the importance of the hydrated interface for facilitating WGS reduction–oxidation mechanisms.

The increased favorability and minimal disruption on the hydrated surface for the reduction of the ceria–zirconia(111) slabs, compared to $CeO_2$ (111), could be attributed to increased covalency and electron delocalization from inclusion of Zr 4d orbitals in the lattice valence band. Electron density maps of the minimized reduced, hydrated $Ce_{0.67}Zr_{0.33}O_2$(111) slab depicted increased interstitial electron density, without apparent increased localization of electron density on any Ce atoms. A localized accommodation of two excess electrons from O removal would require the availability of two reducible Ce neighbors. Combining our observations of the vacancy preference for a maximum of Zr neighbors and the resulting enhanced interatomic Zr–Zr displacement surrounding the vacancies, we speculate that the lattice expansion of Ce–Zr binary oxides during reduction may be due more to the accommodation of the vacancy by local changes in Zr–O coordination, rather than the formation of larger radius $Ce^{3+}$ polarons [42].

### *3.4. Associative complex formation on hydrated oxide surfaces*

When a bifunctional catalyst is exposed to typical WGS reactor conditions, $H_2O$ remains adsorbed on the oxide surface, and CO is preferentially adsorbed on Pt surfaces. Once all Pt adsorption sites are filled, CO adsorption will spill over to the Pt-hydrated oxide interface or to the hydrated oxide itself [8]. Since it has been shown that the adsorption of CO and $H_2O$ are not predisposed by the sequence in which they are introduced to the $CeO_2$ (111) surface and CO adsorption cannot displace $H_2O$ adsorbates [43], any

CO-based adsorption intermediates will be derived from the association of CO with the interfacial hydrated layer. The associative interactions between CO and $H_2O$ are enhanced by electron-withdrawing properties of loaded Pt rafts and the reduction of the oxide surface [43]. Possible associative chemisorption intermediates that could form on a hydrated oxide surface include unidentate or bidentate configurations of formate (HCOO), carboxylate (COOH), and/or carbonate ($CO_3^{2-}$) ligands [11, 44]. These ligands may be actually derived from one another, as intermediates in a sequence of reaction steps. It has been proposed that carbonates are formed from the decomposition of formate ligands, as the final intermediate before $CO_2$ is released [10]. They could represent short-lived associative reaction intermediates. It has been speculated that if a regenerative mechanism is operative that these groups may be spectator species. If that is the case, it is critical to determine whether these complexes impede the final stages of the WGS mechanism, such as the reoxidation of the oxide surface or the release of molecular $H_2$.

*In situ* CIR–FTIR spectroscopic characterization was conducted on WGS surface species formed on ceria–zirconia nanocrystallites at 200 °C, without and with Pt loading. After oxidizing the nanocrystallites in dry air for 2 h and then exposing catalysts to low CO pressures, only weakly adsorbed CO was detected by CIR–FTIR. When the CO pressures were increased to 4 atm or higher, very small amounts of $CO_2$, formates and carbonates were observed, indicating that the catalyst was partially reduced by CO. Under wet, reducing WGS gas conditions (mol%): 6% CO, 30% $H_2O$, 34% $H_2$, and 30% $N_2$, linearly adsorbed CO and a significant amount of formates and carbonates were observed [7]. The formation of carbonates on basic oxides is well known [45]. The larger, more basic $Ce^{3+}$ ions formed under reducing conditions were observed to enhance CO complexation reactions, especially carbonate formation. The formates were weakly bonded and could be removed by outgassing the catalysts in dry nitrogen. The carbonates were only removed by oxidizing the catalyst above 270 °C. Under the wet, reducing WGS conditions on the same oxides with Pt loading, CO linear adsorption was only observed on Pt, and the enhancement of formate and carbonate formation was observed on the oxides. Our CIR–FTIR results supported the hypothesis that the associative formation of carbonates and formates was coupled with the bifunctional regenerative mechanisms that lead to the reduction of the oxide surface. The electron-withdrawing effects of Pt loading under wet, reducing WGS conditions were also found to promote the decomposition of these complexes and the generation of $CO_2$.

We have conducted atomic simulations of CO reaction intermediates on hydrated $CeO_2$ and ceria–zirconia (111) surfaces in order to assess relative stability of these associative reaction intermediates. The CO adsorption enthalpies were determined in kJ $mol^{-1}$ as:

$$\Delta H_{\text{CO ads}} = H_{\text{CO adsorbate complex}} - (H_{\text{hydrated slab}} + H_{\text{CO molecule}}). \quad (3)$$

Here, a more negative adsorption enthalpy indicated a more favorable or exothermic reaction. Carbon monoxide was simulated to adsorb negligibly in the absence [46] and weakly in the presence of 1 ML $H_2O$ on $CeO_2(111)$ (refer to table 4), with no change in the C–O intramolecular distance. The CO adsorbed C down to 2.6 Å above the bare oxide surface and 1.7 Å above the hydrated surface, with the molecular axis tilted from the normal to the surface plane. The binding enthalpy of the weakly electron-donating CO molecule was slightly enhanced by H-bonding interactions with the hydrated layer. On the hydrated $Ce_{0.67}Zr_{0.33}O_2(111)$ surface, CO favorably adsorbed to donate electrons through its HOMO $3\sigma$ orbital to the $H_2O$ molecule displaced from the surface Zr cation. The binding enthalpy is slightly increased (refer to table 4) compared to that on hydrated $CeO_2(111)$. Since the ground state adsorption of CO on these surfaces did not spontaneously lead to the formation of associative complexes, it could be concluded that ligand complexation of the hydrated oxide surfaces was an activated process. It remains unclear whether the reduction of the surface coupled with the electron-withdrawing loaded Pt is necessary for the activation of these chemisorption reactions. If ligand complexation of the oxide surface is locally specific to reduced sites, the CO associative reactions could compete or impede regenerative mechanisms.

**Table 4.** Carbon monoxide adsorption enthalpies, $\Delta H_{\text{CO ads}}$, on (111) slabs with one monolayer $H_2O$.

| Composition Atomic formula | $\Delta H_{\text{CO ads}}$ (kJ $mol^{-1}$ CO adsorbed) | |
|---|---|---|
| | CO Physisorption | CO chemisorption Formate formation |
| $CeO_2$ | −11.6 | −127.4 |
| $Ce_{0.67}Zr_{0.33}O_2$ | −27.0 | −175.6 |
| $Ce_{0.58}Zr_{0.42}O_2$ | −18.8 | −145.7 |

The stability of candidate associative complexes on the hydrated (111) oxide surfaces was assessed by ground state minimizations. If the proposed structure was close to a local minimum in the potential energy surface and remained intact during the minimization, then its relative stability could be determined from the CO physi(chemi)sorption enthalpy. The calculations were not able to identify stable carboxylate or carbonate complexes. However, favorable formation of a unidentate formate complex from the reaction of CO with $H_2O$ was identified consistently for a number of different surface conditions. The CO chemisorption enthalpies for three hydrated surfaces are listed in table 4. The formate complex was tilted to facilitate the interaction of one O with a surface cation and multiple H-bonding interactions with the hydrated layer, as shown schematically in figure 2. Formate complexes have been shown to be stabilized by interactions with coadsorbed $H_2O$ [47]. The remaining H from the $H_2O$ dissociation protonated a nearby lattice surface O. The formate complex did not change appreciably and was slightly stabilized upon surface reduction of hydrated $CeO_2(111)$. The presence of $H_2O$ coadsorbates has been shown to promote the forward dissociation of formates [47]. The most favorable pathway for formate decomposition and $H_2$ desorption has yet to be finalized. So far, we have identified two possible pathways for $H_2$ desorption either by direct formate dissociation to $CO_2$ or through the formation of a unidentate carbonate intermediate.

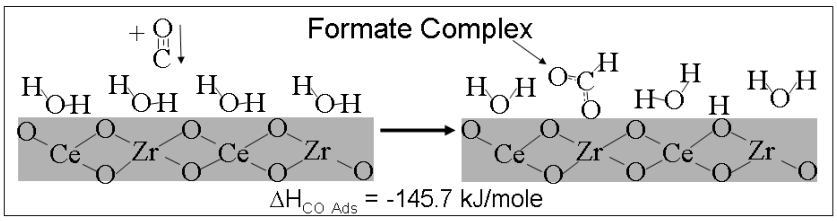


**Figure 2.** Reaction schematic for formate formation on a fully hydrated $Ce_{0.58}Zr_{0.42}O_2(111)$ surface.

**Table 5.** Volumes and enthalpy of substitution, $\Delta H_{substitution}$ for transition metal (TM) doped $Ce_{0.58}Zr_{0.42}O_2$ compositions.

| | TM dopant substitution for Ce | | | TM Dopant substitution for Zr | | |
|---|---|---|---|---|---|---|
| TM dopant | Atomic formula | Volume (Å$^3$/atom) | $\Delta H_{substitution}$ (kJ mol$^{-1}$) | Atomic formula | Volume (Å$^3$/atom) | $\Delta H_{substitution}$ (kJ mol$^{-1}$) |
| — | $Ce_{0.58}Zr_{0.42}O_2$ | 12.4 | — | $Ce_{0.58}Zr_{0.42}O_2$ | 12.4 | — |
| Nb | $Ce_{0.50}Zr_{0.42}Nb_{0.08}O_2$ | 12.4 | 152.6 | $Ce_{0.58}Zr_{0.34}Nb_{0.08}O_2$ | 12.5 | 137.7 |
| Mo | $Ce_{0.50}Zr_{0.42}Mo_{0.08}O_2$ | 12.5 | 323.7 | $Ce_{0.58}Zr_{0.34}Mo_{0.08}O_2$ | 12.6 | 322.6 |
| Ta | $Ce_{0.50}Zr_{0.42}Ta_{0.08}O_2$ | 12.4 | 86.7 | $Ce_{0.58}Zr_{0.34}Ta_{0.08}O_2$ | 12.7 | 201.1 |
| W | $Ce_{0.50}Zr_{0.42}W_{0.08}O_2$ | 12.5 | 347.3 | $Ce_{0.58}Zr_{0.34}W_{0.08}O_2$ | 12.7 | 295.0 |

Both pathways were predicted to require an endothermic input of the order of 100 kJ mol$^{-1}$.

### *3.5. Influence of dopants on the balance of WGS reaction mechanisms*

The spectroscopy and modeling results supported the hypothesis that associative reaction cycles could be very competitive with regenerative cycles on hydrated ceria-based surfaces. Further analysis of our modeling revealed that in ceria and ceria–zirconia, formate complex formation was very close in energy to reoxidation of a reduced surface (compare the negative of the ceria–zirconia reduction values in table 3 to the formate formation values in table 4). From our kinetic analyses of ceria–zirconia catalyst performance along with the low temperature TPR observations [2], it was hypothesized that lattice reduction was not the rate-limiting step, but rather reoxidation. Here, the rate at which O could be removed from the lattice outstripped the rate at which $H_2O$ could chemisorb and react to replenish O. One hypothesis was that this was due to the formation of very stable intermediate competitor spectator species which locked up active sites on the surface. Thus, a strategy was adopted to shift the WGS oxidation–reduction balance towards reoxidation and to increase the support electronic conductivity by introducing dopants with different valences, ionization energies, and acid/base character. Here, we sought to add less reducible species to make reoxidation more favorable. The acidic transition metal (TM) dopants, listed in terms of increasing acidity or ionization energy: Nb, Mo, Ta, and W, were selected for investigation. They are strong electron acceptors and are fully oxidized in their Lewis acid-like oxide phases with generally empty d orbitals ($d^0$ oxides).

It is often possible to utilize ceria–zirconia nanocrystallites co-precipitated with stable low loadings of thermodynamically insoluble dopants, because phase separation is kinetically impeded at the relatively low temperatures used for synthesis and reactor operation. Predictions were made of the enthalpy of substitution, $\Delta H_{substitution}$, of 0.08 at.% of selected TM dopants for either Ce or Zr in the $Ce_{0.58}Zr_{0.42}O_2$ composition, where $\Delta H_{substitution}$ was determined in kJ mol$^{-1}$ from the relationship:

$$\Delta H_{substitution} = H_{doped\ oxide} + H_{displaced\ atom} - (H_{undoped\ oxide} + H_{dopant\ atom}) \quad (4)$$

where the atomic energies were determined from the standard state bulk phases. Table 5 shows that in all cases, the enthalpies of substitution were predicted to be endothermic. Locally the dopants assumed a dodecahedral coordination with the eight neighboring O atoms, distorting the cubic cation coordination with eight O in the native lattice. In this structural arrangement, each O gathers electrons from four cations, so that in the fully oxidized doped bulk lattice, the actual dopant formal charge is 4+, as opposed to the 5+ or 6+ formal charge assumed in the octahedral coordination in their respective pure oxides. It can be seen from table 5 that Nb substitution introduced the smallest volume change. Density of state analyses showed that the dopant interactions enhanced hybridization of the oxide valence band, promoting covalency and delocalization of excess electronic charge. In addition, the excess electrons of the transition metal dopants in their lower oxidation states partially filled the conduction band, improving electronic conductivity.

Hydrated doped ceria–zirconia(111) slab models were used to simulate tuning the balance of regenerative WGS reactions with dopants. The compositions equivalent to the stoichiometries in table 5 with the TM dopant substituted for Ce, $Ce_{0.50}Zr_{0.42}TM_{0.08}O_2$, were selected for further investigation by atomic simulation, and by synthesis following the procedures described in [2]. The most favorable slab configurations revealed the dopant atom at the surface. When these were minimized with 1 ML $H_2O$, the $H_2O$ molecule

**Table 6.** Average $H_2O$ adsorption enthalpies, $\Delta H_{\text{ads } H_2O}$, for one monolayer $H_2O$ on transition metal-doped ceria–zirconia (111) slabs, and qualitative descriptions of changes in the hydrated surface layer.

| Atomic formula | $\Delta H_{\text{ads } H_2O}$ (kJ mol$^{-1}$) | Description of hydrated layer |
|---|---|---|
| $CeO_2$ | −52.4 | Regular, ice-like configuration, $H_2O$ O lone pair interaction with cation |
| $Ce_{0.58}Zr_{0.42}O_2$ | −57.7 | $H_2O$ displaced over Zr, H-bonded with adjacent O |
| $Ce_{0.50}Zr_{0.42}Nb_{0.08}O_2$ | −79.4 | $H_2O$ dissociated to hydroxylate Nb, other $H_2O$ shifted and tilted |
| $Ce_{0.50}Zr_{0.42}Mo_{0.08}O_2$ | −82.3 | $H_2O$ dissociated to hydroxylate Mo, other $H_2O$ shifted and tilted |
| $Ce_{0.50}Zr_{0.42}Ta_{0.08}O_2$ | −90.2 | $H_2O$ dissociated and subsurface vacancy formed to hydroxylate Ta and Zr |
| $Ce_{0.50}Zr_{0.42}W_{0.08}O_2$ | −110.4 | $H_2O$ dissociated to protonate 2 lattice O and oxidize W, 1 $H_2O$ displaced |

dissociated over the dopant to hydroxylate the dopant and to protonate the adjacent lattice surface O, as summarized in table 6. The trend observed was that the $\Delta H_{\text{ads } H_2O}$ became more favorable and the interaction of the hydrated layer with the substrate became more complex as the dopant acidity increased. These $H_2O$ acid–base reactions set the stage for shifting the equilibrium of the WGS reactions.

Even a very small amount of the acidic TM dopants had a significant impact on oxidation–reduction behavior of the ceria–zirconia lattice. The substituted dopants were in an atypically low valence or oxidation state compared to that in their native oxides. The removal of an additional O was very costly, even from the most favorable location, so that the reduction enthalpies of the TM-doped lattices were significantly more endothermic than for the undoped lattice. The opposing reoxidation of reduced doped lattices, which was of interest in the current study, was predicted to be extremely favorable compared to that of the undoped compositions. The predicted reoxidation enthalpies are compared in table 7, and became more favorable with increasing dopant acidity.

The WGS species on Pt-loaded mixed metal oxide crystallites were characterized by CIR–FTIR under the wet reducing WGS 30% CO, 30% $H_2O$, 34% $H_2$, 6% $N_2$ gas fed molar composition at 200 °C and 2 atm. Significant reductions in formate and/or carbonate adsorbances were observed over the 1300–1600 cm$^{-1}$ wavenumber range on a Pt-loaded composition doped with a low Mo loading, $Ce_{0.70}Zr_{0.20}Mo_{0.10}O_2$ [7]. These experimental results supported the hypothesis that the associative formation of carbonates and formates was coupled with the reduction of the oxide surface by the regenerative mechanism and that the acidic dopants catalyze the forward formate decomposition mechanism.

Predictions were used to survey tuning of the balance with the coupled regenerative WGS reaction steps for CO oxidation and for $H_2O$ reduction through the reformulation with the acidic TM dopants. The coupled reaction predictions given in table 8 were determined by combining the $\Delta H_{\text{reduction}} = -\Delta H_{\text{reoxidation}}(\Delta H_{\text{reoxidation}})$ values in table 7 with the gas phase predicted reaction enthalpies for CO oxidation ($H_2O$ reduction). The TM dopants are predicted to shift the CO oxidation coupled with support reduction to become less favorable and to shift the $H_2O$ reduction coupled with the support reoxidation to become more favorable. The favorability of these opposing reactions was predicted to be the most balanced for the addition of the Ta and Mo dopants. Here, the competing undesired reverse reaction for $H_2$ oxidation to water became unfavorable. Also, the surface reoxidation is significantly more favorable than the reaction of $H_2O$ with CO to form stable formate complexes (compare tables 4 and 7). This may explain the lower amount of formate complexation observed by CIR–FTIR.

**Table 7.** Next-nearest neighbor cations in most favorable subsurface vacancies and reoxidation enthalpies, $\Delta H_{\text{reoxidation}}$, for reduced undoped and doped ceria–zirconia compositions.

| 1 ML hydrated Reduced composition | Subsurface O vacancy Next-nearest neighbors | $\Delta H_{\text{reoxidation}}$ [a] (eV) |
|---|---|---|
| $Ce_{0.58}Zr_{0.42}O_{1.96}$ | 3 Zr and 1 Ce | −134.0 |
| $Ce_{0.50}Zr_{0.42}Nb_{0.08}O_{1.92}$ | 3 Zr and 1 Ce | −263.5 |
| $Ce_{0.50}Zr_{0.42}Mo_{0.08}O_{1.92}$ | 3 Zr and 1 Mo | −340.1 |
| $Ce_{0.50}Zr_{0.42}Ta_{0.08}O_{1.92}$ | 3 Zr and 1 Ta | −369.0 |
| $Ce_{0.50}Zr_{0.42}W_{0.08}O_{1.92}$ | 3 Zr and 1 W | −459.5 |

[a] Reoxidation: $Ce_{(1-x-y)}TM_{(y)}Zr_{(x)}O_{1.92} * 4H_2O + \frac{1}{2}O_2 \rightarrow Ce_{(1-x-y)}TM_{(y)}Zr_{(x)}O_2 * 4H_2O$.

A schematic of the complete simulated regenerative WGS reaction cycle on $Ce_{0.50}Zr_{0.42}Ta_{0.08}O_2$, including the CO adsorption energy and $CO_2$ product desorption energy, is shown in figure 3 along with the CO oxidation and $H_2O$ reduction steps coupled with the support reduction and reoxidation, respectively. Included in this cycle is the 55.0 kJ mol$^{-1}$ desorption energy for $CO_2$ after it is formed. While the energy of the overall WGS reaction cannot change, the acidic TM dopants are predicted to shift the relative balance of the reaction steps, enhancing the refilling of oxide vacancies and $H_2$ generation, and minimizing the blocking of sites by associative complex formation. The total ground state, uncorrected VASP-calculated reaction enthalpy of −36.6 kJ mol$^{-1}$ for the regenerative WGS reaction cycle compares well with the gas phase WGS reaction value of $\Delta G = -38.2$ kJ mol$^{-1}$ calculated at 50 K from measured thermodynamic data [48].

The catalyst compositions were evaluated by measuring CO conversion under high temperature WGS conditions, using the wet reducing gas molar composition: 4.9% CO, 10.5% $CO_2$, 33% $H_2O$ and 30.3% $H_2$. The catalysts (0.2 cm$^3$) were packed with inert alumina in a 5 cm$^3$ reactor, run under a gas flow of 1000 cm$^3$ min$^{-1}$ or 300 000 h$^{-1}$ space velocity [5]. The Mo-doped ceria–zirconia catalyst composition, $Pt/Ce_{0.70}Zr_{0.2}Mo_{0.10}O_2$, exhibited higher CO conversion (of the order of a 20% increase) at low temperatures compared to replicated tests of undoped or La doped catalysts with comparable Pt loadings [2], as shown in figure 4. The CO turnover data were measured during the initial catalyst

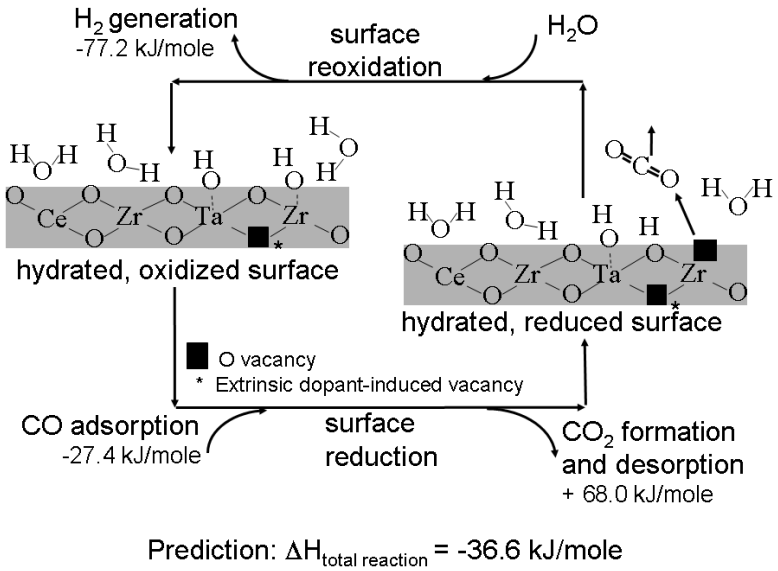


**Figure 3.** Schematic diagram of the regenerative water gas shift reaction cycle on fully hydrated $Ce_{0.50}Zr_{0.42}Ta_{0.08}(111)$.

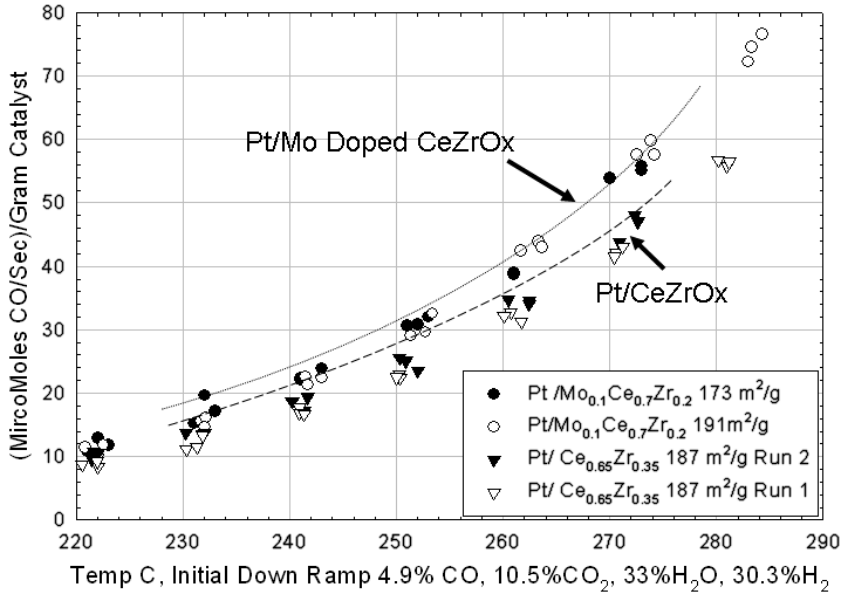


**Figure 4.** Comparison water gas shift CO conversion tests for duplicate runs of $Pt/Ce_{0.65}Zr_{0.35}O_2$ baseline catalyst with two runs from separate $Pt/Ce_{0.70}Zr_{0.2}Mo_{0.10}O_2$ catalyst syntheses.

**Table 8.** Combined regenerative water gas shift reaction enthalpies for the undoped and doped ceria–zirconia supports with one monolayer $H_2O$ for the support reduction reaction coupled with CO oxidation to $CO_2$, and support reoxidation with $H_2O$ reduction to $H_2$.

| 1 ML $H_2O$ hydrated composition atomic formula | Support reduction and CO oxidation ($CO + \frac{1}{2}O_2 \rightarrow CO_2$) $\Delta H_{(\text{support reduction \& CO oxidation})}$ (kJ mol$^{-1}$) | Support reoxidation and $H_2O$ reduction ($H_2O \rightarrow H_2 + \frac{1}{2}O_2$) $\Delta H_{(\text{support reoxidation \& } H_2O \text{ reduction})}$ (kJ mol$^{-1}$) |
|---|---|---|
| $CeO_2$ | −214.5 | 150.3 |
| $Ce_{0.58}Zr_{0.42}O_2$ | −222.0 | 157.8 |
| $Ce_{0.50}Zr_{0.42}Nb_{0.08}O_2$ | −92.5 | 28.3 |
| $Ce_{0.50}Zr_{0.42}Ta_{0.08}O_2$ | 13.0 | −77.2 |
| $Ce_{0.50}Zr_{0.42}Mo_{0.08}O_2$ | −15.9 | −48.3 |
| $Ce_{0.50}Zr_{0.42}W_{0.08}O_2$ | 103.5 | −167.7 |

down ramp from 400 °C, where the data were collected at each temperature step for 1 h. Kinetic rate analyses for the CO conversion yielded reaction orders approaching 0 for CO and 1 for $H_2O$, most likely due to the optimization of the regenerative WGS mechanism.

## 4. Conclusion

Effective micro-engineered Pt/ceria–zirconia WGS catalysts having a large surface area with a high density of active sites were developed from coordinated atomic modeling, catalyst synthesis, structural characterization, kinetic performance tests, and micro-kinetic reaction analyses. Atomic modeling was used to interpret probable ligand complexation and blocking of active ceria–zirconia surface sites via the associative WGS reaction mechanism from *in situ* spectroscopy results. Atomic modeling screening of new ceria–zirconia catalyst formulas with acidic TM dopants, including: Nb, Mo, Ta, and W, predicted an increased favorability for reoxidation of the ceria–zirconia lattice via the regenerative WGS mechanism. The predictions were used to develop doped ceria–zirconia compositions that provided the optimum tuning and balance of regenerative WGS reactions. *In situ* characterization, kinetics testing, and micro-kinetics analyses demonstrated the improved performance of newly designed Mo-doped Pt/ceria–zirconia catalysts, which experimentally exhibited higher CO turnover rates compared to the undoped ceria–zirconia.

## Acknowledgments

This work was fostered by the UTRC Compact FPS Team, which in addition to the co-authors included Zissis Dardas (project leader), Harry Cordatos, Fangxia Feng, Miriam Leffler, Caroline Newman, Xia Tang, and Fabien Wijzien. The steadfast support of Susan D Brandes for the integration of atomic modeling with experimentation in new scientific endeavors is gratefully acknowledged. This work was supported by HydrogenSource, a joint venture between United Technologies Corporation and Shell.

## References

[1] Bunluesin T, Gorte R J and Graham G W 1998 Studies of the water–gas-shift reaction on ceria-supported Pt, Pd, and Rh: implications for oxygen-storage properties *Appl. Catal.* B **15** 107–14

[2] Vanderspurt T H, Wijzen F, Tang X, Leffler M P, Willigan R R, Newman C A, Radhakrishnan R, Feng F, Laube B L, Dardas Z, Opalka S M and She Y 2007 Ceria-based mixed-metal oxide structure, including method of making and use *US Patent Specification* 7166263

[3] Vanderspurt T H and Willigan R R 2006 Durable catalyst for processing carbonaceous fuel, and the method of making *US Patent Specification* 104805 A2

[4] Willigan R R, Radhakrishnan R, Cordatos H, Opalka S M, Dardas Z and Vanderspurt T H 2004 Root-cause analysis and mitigation of high temperature water gas shift deactivation mechanisms *Proc. Div. Petroleum Chem., 227th ACS Nat. Mtg*

[5] Radhakrishnan R, Willigan R R, Dardas Z and Vanderspurt T H 2006 Water gas shift activity of noble metals supported on ceria–zirconia oxides *AIChE J.* **52** 1888–94

[6] Radhakrishnan R, Willigan R R, Dardas Z and Vanderspurt T H 2006 Water gas shift activity and kinetics of Pt/Re catalysts supported on ceria–zirconia oxides *Appl. Catal.* B **66** 23–8

[7] Feng F 2004 Synthesis of proton conducting mesoporous materials and composite membranes for high temperature proton exchange membrane fuel cells *PhD Dissertation* The University of Texas at Dallas

[8] Hilaire S, Wang X, Luo T, Gorte R J and Wagner J 2001 A comparative study of water–gas-shift reaction over ceria supported metallic catalysts *Appl. Catal.* A **215** 271–8

[9] Li Y, Fu Q and Flytzani-Stephanopoulos M 2000 Low-temperature water–gas shift reaction over Cu- and Ni-loaded cerium oxide catalysts *Appl. Catal.* B **27** 179–91

[10] Shido T and Iwasawa Y 1993 Reactant-promoted reaction mechanism for water–gas shift reaction on Rh-doped $CeO_2$ *J. Catalysis* **141** 71–81

[11] Barbier J and Duprez D 1994 Review: steam effects in three-way catalysts *Appl. Catal.* B **4** 105–40

[12] Kresse G and Hafner J 1993 *Ab initio* molecular dynamics for liquid metals *Phys. Rev.* B **47** 558–61

[13] Kresse G and Furthmuller J 1996 Efficiency of *ab initio* total energy calculations for metals and semiconductors using a plane-wave basis set *Comput. Mater. Sci.* **6** 15–50

[14] Kresse G and Furthmuller J 1996 Efficient iterative schemes for *ab initio* total energy calculations using a plane wave basis set *Phys. Rev.* B **54** 11169–86

[15] Kresse G and Joubert D 1999 From ultrasoft pseudopotentials to the projector augmented wave method *Phys. Rev.* B **59** 1758–75

[16] Perdew J and Wang Y 1992 Generalized gradient approximation for the exchange–correlation hole of a many-electron system *Phys. Rev.* B **46** 6671–87

[17] Kepinski L and Wolcyrz M 1992 Rietveld refinement of the structure of CeOCl formed in $Pd/CeO_2$ catalyst: notes on the existence of a stabilized tetragonal phase of $La_2O_3$ in La–Pd–O system *J. Solid State Chem.* **99** 409–13

[18] Angelov B M 1981 Energies and electronic energy levels of lanthanide dioxides *J. Phys. C: Solid State Phys.* **14** L757

[19] Nakajima A, Yoshihara A and Ishigame M 1994 Defect-induced Raman spectra in doped cerium oxide ($CeO_2$) *Phys. Rev.* B **50** 13297–307

[20] Conesa J C 1995 Computer modeling of surfaces and defects on cerium dioxide *Surf. Sci.* **329** 337–52

[21] Gennard S, Curia F and Catlow C R A 1999 Comparison of bulk and surface properties of ceria and zirconia by *ab initio* investigations *J. Phys. Chem.* B **103** 10158–70

[22] Liu G, Rodriguez J A, Hrbek J and Dvorak J 2001 Electronic and chemical properties of $Ce_{0.8}Zr_{0.2}O_2(111)$ Surfaces: photoemission, XANES, density-functional, and $NO_2$ adsorption studies *J. Phys. Chem.* B **105** 7762–70

[23] Skorodumova N V, Ahuja R, Simak S I, Abrikosov I A, Johansson B and Lundqvist B I 2001 Electronic, bonding, and optical properties of $CeO_2$ and $Ce_2O_3$ from first principles *Phys. Rev.* B **64** 115108

[24] Koelling D D, Boring A M and Wood J H 1983 The electronic structure of $CeO_2$ and $PrO_2$ *Solid State Commun.* **47** 227–32

[25] Yashmina M, Morimoto K, Ishizawa N and Yashimura M 1993 Diffusionless tetragonal–cubic transformation temperature in zirconia–ceria solid solutions *J Am. Ceram. Soc.* **76** 2865–8

[26] Kaspar J and Fornasiero P 2002 Structural properties and thermal stability of ceria–zirconia and related materials *Catalysis by Ceria and Related Materials* ed A Trovarelli (London: Imperial College Press) pp 217–41

[27] Kim J D 1989 Lattice parameter, ionic conductivities, and solubility limits in fluorite-structure $MO_2$ oxide *J. Am. Ceram. Soc.* **72** 1415–21

[28] Balducci G, Islam M S, Kaspar J, Fornasiero P and Graziani M 2000 Bulk reduction and oxygen migration in the ceria-based oxides *Chem. Mater.* **12** 677–81
[29] Vlaic G, Fornasiero P, Geremia S, Kaspar J and Graziani M 1997 Relation between the zirconia-promoted reduction in the Rh-loaded $Ce_{0.50}Zr_{0.50}O_2$ mixed oxide and the Zr–O local structure *J. Catalysis* **168** 386–92
[30] Fornasiero P, Balducci G, Di Monte R, Kaspar J, Sergo V, Gubitosa G, Ferrero A and Graziani M 1996 Modification of the redox behavior of $CeO_2$ induced by structural doping with $ZrO_2$ *J. Catalysis* **164** 173–83
[31] Duprez D and Descorme C 2002 Oxygen storage/redox capacity and related phenomena on ceria-based catalysts *Catalysis by Ceria and Related Materials* ed A Trovarelli (London: Imperial College Press) pp 243–80
[32] Taft C A, Longo E, Sensato F, Martins J B L, Sambrano R, Almeida A L and Lester W A 2000 Interaction of water, gases and other complexes with metal oxide surfaces *Recent Res. Dev. Quantum Chem.* **1** 105–30
[33] Ahdjoudj J and Minot C 1998 Adsorption of $H_2O$ on metal oxides: a periodic *ab initio* investigation *Surf. Sci.* **402–404** 104–9
[34] Goniakowski J and Gillan M J 1996 The adsorption of $H_2O$ on $TiO_2$ and $SnO_2$(110) studied by first principles calculations *Surf. Sci.* **350** 145–58
[35] Kumar S and Schelling P K 2006 Density functional theory study of water adsorption at reduced and stoichiometric ceria (111) surfaces *J. Chem. Phys.* **125** 204704–11
[36] Goniakowski J and Noguera C 1995 Theoretical investigation of hydroxylated oxide surfaces *Surf. Sci.* **330** 337–49
[37] Kaspar J, Fornasiero P and Graziani M 1999 Use of $CeO_2$-based oxides in three-way catalysts *Catal. Today* **50** 285–98
[38] de Carolis S, Pascual J L, Pettersson L G M, Baudin M, Wojcik M, Hermansson K, Palmqvist A E C and Muhammed M 1999 Structure and electronic properties of Ca-doped $CeO_2$ and implications on catalytic activity: an experimental and theoretical study *J. Phys. Chem.* B **103** 7627–36
[39] Janvier C, Pijolat M, Valdiveso F and Soustelle M 2000 Thermodynamic description of the nonstoichiometric defect structure in $Ce_{1-x}Zr_xO_2$ solid solution powders *Solid State Ion.* **127** 207–22
[40] Shapovalov V and Metiu H 2007 Catalysis by doped oxides: CO oxidation by $Au_xCe_{1-x}O_2$ *J. Catalysis* **245** 205–14
[41] Yang Z, Woo K W and Hermansson K 2006 Adsorption of NO on unreduced and reduced $CeO_2$ surfaces: a plane-wave DFT study *Surf. Sci.* **600** 4953–60
[42] Mogensen M, Sammes N M and Tompsett G A 2000 Physical, chemical and electrochemical properties of pure and doped ceria *Solid State Ion.* **129** 63–94
[43] Kundakovic L, Mulins D R and Oberbury S H 2000 Adsorption and reaction of $H_2O$ and CO on oxidized and reduced $Rh/CeO_x$(111) surfaces *Surf. Sci.* **457** 51–62
[44] Emiroglu S, Barsan N, Weimar U and Hoffmann V 2001 *In situ* diffuse reflectance infrared spectroscopy study of CO adsorption on $SnO_2$ *Thin Solid Films* **391** 176–85
[45] Henrich V E and Cox P A 1994 *The Surface Science of Metal Oxides* (Cambridge: Cambridge University Press)
[46] Yang Z, Woo K W and Hermansson K 2004 Strong and weak adsorption of CO on $CeO_2$ surfaces from first principles calculations *Chem. Phys. Lett.* **396** 384–92
[47] Shido T, Yamaguchi A, Asakura K and Iwasawa Y 2000 Surface catalytic reactions assisted by gas phase molecules: activation of reaction intermediates *J. Mol. Catal.* **163** 67–77
[48] Roine A *HSC Chemistry 5.11* copyright Outokumpu Research Oy Pori, Finland